

Two-Dimensional Perovskite Chiral Ferromagnets

Bing Sun, Xiao-Fei Liu, Xiang-Yang Li, Yamin Zhang, Xiangfeng Shao,* Dezheng Yang,* and Hao-Li Zhang*



Cite This: *Chem. Mater.* 2020, 32, 8914–8920



Read Online

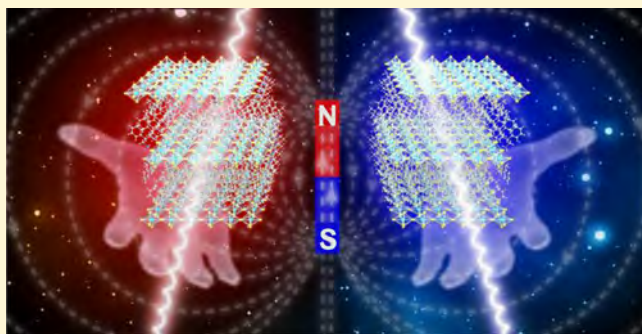
ACCESS |

Metrics & More

Article Recommendations

Supporting Information

ABSTRACT: Magnetic molecular materials with a chiral configuration are attractive candidates for sensing, information storage, and spintronics. Herein, we report the first example of two-dimensional hybrid perovskite chiral ferromagnets, $(R\text{-MPEA})_2\text{CuCl}_4$ and $(S\text{-MPEA})_2\text{CuCl}_4$. These two compounds exhibit strong oppositely signed circular dichroism signals and clear ferromagnetic behaviors. Magnetic measurements revealed high saturation magnetization up to 12.5 emu g^{-1} . The coexistence of strong chirality and ferromagnetism enabled successful study on their magneto-chiral dichroism spectra. These findings demonstrate a new materials platform for future magneto-optical and spintronic applications, providing insights to the structure–property correlation of chiral ferromagnetic perovskite.



INTRODUCTION

Great efforts have been devoted to the material systems whose time-reversal and space-inversion symmetries are simultaneously broken, i.e., in a medium with magnetism and chirality.¹ Magnetism and chirality are directly connected through an antisymmetric exchange of Dzyaloshinskii–Moriya interaction (DMI). In a chiral ferromagnet, chirality breaks the space inversion and mirror symmetry,² which contributes to new types of interesting cross-effects, such as chiral magnetic effect (CME),³ chiral-induced spin selectivity⁴ (CISS), and magneto-chiral dichroism (MChD).⁵ Materials with both magnetism and chirality properties can be central to fundamental advances in multiferroics, current-induced spin–orbit torque, and topological magnetic structures.⁶

Chiral ferromagnets may play a crucial role in spintronic devices, as a spin-polarized current flowing through chiral magnetic structures will cause a variety of excitations or manipulations of the magnetization.⁷ The interplay between crystallographic chirality and magnetism also enables physical insight into fundamental understanding of anomalous Hall effect (AHE), magnetization-induced second-harmonic generation (MSHG) and MChD, and can give rise to new quantum particles, such as skyrmions.⁸ Chiral ferromagnetic systems possessing DMI are of fundamental interest in the field of molecular magnetism,⁹ and is becoming more important for new applications in spintronics.¹⁰ However, the examples of chiral ferromagnets are still very limited.^{11–15}

Recently, organic–inorganic hybrid perovskites have been explored as a platform for developing new multifunctional materials.^{16–20} Metal-halide octahedra form layers separated by the organic molecules, these materials are commonly referred

to as two-dimensional (2D) hybrid perovskites.²¹ 2D hybrid perovskites have been exploited in a wide range of applications, owing to their multiple-quantum-well structures, relatively high stability, and impressive compositional tunability. Very few ferromagnetic perovskites have been prepared so far, which showed some interesting properties, such as spin-reorientation²² and thermochromic ferromagnets.²³ The unique structural tunability of hybrid perovskites offers an unprecedented opportunity to directly incorporate chiral organic molecules to enable perovskite's chirality.^{24–28} It has been demonstrated that spin-polarized photoluminescence occurred in chiral perovskites without an external magnetic field.²⁹ Spin transport in perovskite can be effectively manipulated upon the chirality of the $(R/S\text{-rac-MBA})_2\text{PbI}_4$ via the CISS mechanism.⁴ Moreover, large spin–orbit coupling (SOC),³⁰ controllable Rashba splitting,^{31,32} large Stark effect,^{33,34} and optical spin selection³⁵ have been discovered in hybrid perovskites, highlighting their potential in spin-based applications. Theoretical investigations have predicted more attractive applications of chiral perovskite in quantum informatics and spintronics.^{36,37}

Despite extensive investigations, perovskite chiral ferromagnets remain blank to date. Herein, for the first time, we synthesized a pair of enantiomeric 2D hybrid perovskites, $(R\text{-MPEA})_2\text{CuCl}_4$ and $(S\text{-MPEA})_2\text{CuCl}_4$, which exhibit strong oppositely signed circular dichroism signals and clear ferromagnetic behaviors. Magnetic measurements revealed high saturation magnetization up to 12.5 emu g^{-1} .

Received: June 29, 2020

Revised: August 26, 2020

Published: August 26, 2020



$(MPEA)_2CuCl_4$ and $(S\text{-}MPEA)_2CuCl_4$. Circular dichroism (CD) and magnetic measurements confirm that these two perovskites possess both chirality and ferromagnetism. MChD investigation on chiral perovskites was carried out for the first time, which revealed potential of these materials for future optomagnetic and spintronic applications.

Direct combination of the chiral cations and $CuCl_2\cdot 2H_2O$ mixing in ultrapure water at 80 °C followed by slow cooling of the solutions to room temperature yields yellow flake crystals, as seen in Figure 1a,b. Detailed synthesis procedures are listed

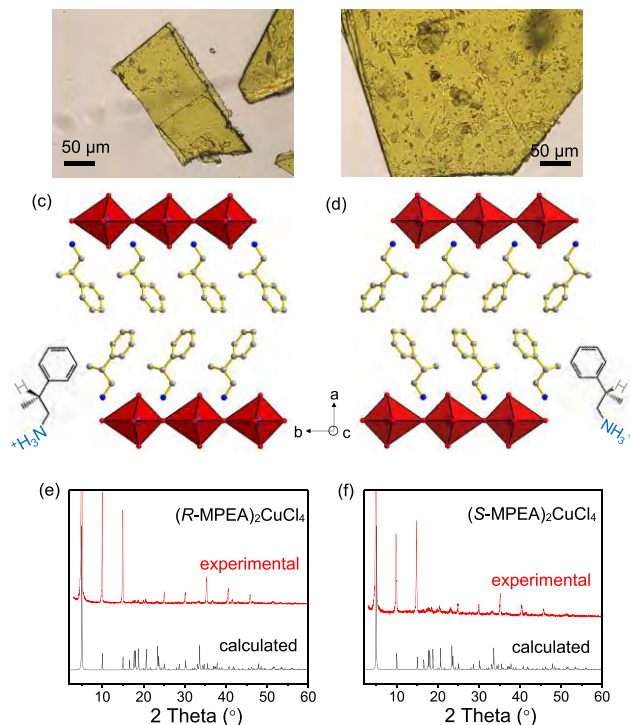


Figure 1. Optical microscopic images of $(R\text{-}MPEA)_2CuCl_4$ (a) and $(S\text{-}MPEA)_2CuCl_4$ (b). Single crystal structures viewed along the c -axis ($R\text{-}MPEA)_2CuCl_4$ (c) and $(S\text{-}MPEA)_2CuCl_4$ (d) with color codes Cu (Indigo), Cl (Red), C (gray), and N (blue). The $CuCl_6$ -units are displayed as polyhedra, H atoms are omitted for clarity. Experimental and calculated powder X-ray diffraction (PXRD) patterns of (e) $(R\text{-}MPEA)_2CuCl_4$ and (f) $(S\text{-}MPEA)_2CuCl_4$.

in the [Experimental Section](#). The crystal structure and refinement data are provided in Figure 1c,d and Table S1 of the [Supporting Information \(SI\)](#). Powder X-ray diffraction (PXRD) patterns of $(R\text{-}MPEA)_2CuCl_4$ and $(S\text{-}MPEA)_2CuCl_4$ all exhibit sharp peaks and show almost identical features as simulated spectra based on their single crystal structures, confirming the phase purity of the as-synthesized crystals (Figure 1e,f). Thermogravimetric analysis (TGA) measurements indicate that $(R\text{-}MPEA)_2CuCl_4$ and $(S\text{-}MPEA)_2CuCl_4$ possesses high thermal stability, with identical decomposition temperature above 450 K, while $(rac\text{-}MPEA)_2CuCl_4$ is thermally stable up to 440 K (Figure S1).

Figure 1c,d illustrates the single-crystal structures of the $(R\text{-}MPEA)_2CuCl_4$ and $(S\text{-}MPEA)_2CuCl_4$. Both crystals have 2D layered structures, in which the successive corner-sharing inorganic $[CuCl_6]^{4-}$ octahedral layer is intercalated by two layers of chiral organic cations. In such a way, the multiple-quantum-wells structure is naturally formed with the chiral molecules embedded in ref 38. Compounds $(R\text{-}MPEA)_2CuCl_4$

and $(S\text{-}MPEA)_2CuCl_4$ are antisymmetrically isostructural and crystallize in the chiral space group of $C2$ assigned to the monoclinic crystal system. The lattice parameters of $(R\text{-}MPEA)_2CuCl_4$ and $(S\text{-}MPEA)_2CuCl_4$ are $a = 35.470 \text{ \AA}$, $b = 5.4017 \text{ \AA}$, and $c = 5.3432 \text{ \AA}$; and $a = 35.450 \text{ \AA}$, $b = 5.4065 \text{ \AA}$, and $c = 5.3466 \text{ \AA}$, respectively.

It is known that the Cu^{2+} ions in the perovskite structure are strongly Jahn–Teller (JT) active, giving rise to changes in the Cu–Cl bond lengths and hence to structural distortions of the $CuCl_6$ octahedra.³⁹ The distortion levels (Δd) of the individual $[CuCl_6]^{4-}$ octahedron is calculated using eq 1:

$$\Delta d = \frac{1}{6} \sum \left[\frac{d_n - d}{d} \right]^2 \quad (1)$$

where d is the mean Cu–Cl bond length (Tables S2 and S3), and d_n represents the six individual Cu–Cl bond lengths.⁴⁰ The distortions of $CuCl_6$ octahedral in the perovskite structure are listed in Table S4. The values of Δd is calculated to be 3.32×10^{-4} and 3.07×10^{-4} for the $(R\text{-}MPEA)_2CuCl_4$ and $(S\text{-}MPEA)_2CuCl_4$, respectively, indicating that there is no substantial difference in structural distortion.

UV-vis-NIR absorption spectra of $(R\text{-}MPEA)_2CuCl_4$, $(S\text{-}MPEA)_2CuCl_4$, and racemic compound are shown in Figure 2a, which are nearly identical. The absorption peak at ~ 379

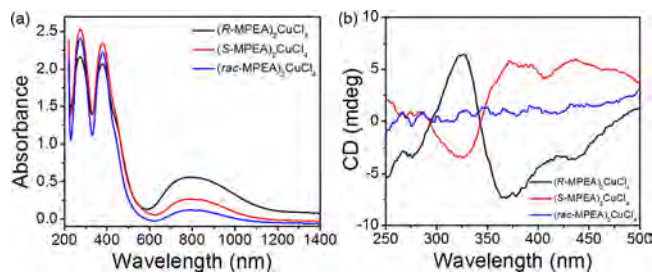


Figure 2. Absorbance and CD spectra of the chiral perovskites. UV-vis-NIR absorption spectra (a) and CD spectra (b) of $(R\text{-}MPEA)_2CuCl_4$, $(S\text{-}MPEA)_2CuCl_4$, and $(rac\text{-}MPEA)_2CuCl_4$.

nm near the absorption edge corresponds to the 2D perovskite excitonic feature, which is characteristic for 2D perovskites. The 2D hybrid perovskite structures are natural quantum wells with semiconducting slabs alternating with dielectric slabs.⁴¹ Therefore, this absorption feature is derived from quantum and dielectric confinement effects of the carriers, previously shown in other 2D semiconductors such as the $(CH_3CH_2NH_3)_4Pb_3Br_{10-x}Cl_x$ series and $(PA)_2(MA)_{n-1}Pb_nI_{3n+1}$.^{42,43} The high energy absorption band observed at ~ 274 nm is associated with $\pi \rightarrow \pi^*$ transition of the organic cations.⁴⁴ The absorption edges of the chiral perovskites locate around 567 nm. A broad band appears in the near-infrared spectrum ranging from 600 to 1200 nm, indicating the appearance of broad gap states.⁴⁵ This weak, broad band centered at approximately 800 nm in the absorption spectra results from Laporte forbidden Cu^{2+} $d-d$ transitions.^{46,47} Photoluminescence spectra of $(R\text{-}MPEA)_2CuCl_4$, $(S\text{-}MPEA)_2CuCl_4$ and $(rac\text{-}MPEA)_2CuCl_4$ are shown in Figure S2. A broad emission band peaking at 555 and 617 nm was observed for these three compounds, indicating that nearly identical photoluminescence properties.

Figure 2b reveals strong CD signals that appear at the same wavelengths (at 324, 372, and 436 nm) for the $(R\text{-}MPEA)_2CuCl_4$ and $(S\text{-}MPEA)_2CuCl_4$ films but with opposite

signs, while $(rac\text{-MPEA})_2\text{CuCl}_4$ shows a featureless flat signal. The CD spectra indicate strong chirality of the two new 2D perovskites. As shown in Figure S3, opposite CD absorption features are observed in $R\text{-MPEA}\cdot\text{HCl}$ and $S\text{-MPEA}\cdot\text{HCl}$. The racemic blend of $rac\text{-MPEA}\cdot\text{HCl}$ exhibits no absorption difference between left- and right-handed polarized light. The CD signals for these chiral organic ammonium salts mainly located before 300 nm. However, when they are incorporated into the chiral perovskite, the resulting perovskites exhibit strongly opposite CD values in the visible region (Figure 2b). These observations indicate that the chirality of organic cations directly transferred to the perovskite framework, thereby endowing the corresponding 2D perovskites with intrinsic chirality.⁴⁸ Notably, the CD peaks were located before the absorption edge at 567 nm, suggesting a lifting of the spin degeneracy within the band edge electronic states induced by the chiral molecules.⁴

Temperature-dependent magnetic susceptibility in a 100 Oe magnetic field for the $(R\text{-MPEA})_2\text{CuCl}_4$, $(S\text{-MPEA})_2\text{CuCl}_4$, and $(rac\text{-MPEA})_2\text{CuCl}_4$ clearly show the transition from ferromagnet to paramagnet (Figure 3a). A long-range

hybrid perovskites. From the configuration of Cu $d_{x^2-y^2}$ orbitals in the Cu–Cl octahedral layer (Figure S4), each octahedron is prolonged along the Jahn–Teller z -axis that lies in the CuCl plane. In an organic–inorganic perovskite system, the magnetic spin originates from the unoccupied Cu $d_{x^2-y^2}$ orbital.⁵¹ For these hybrid perovskites, the $d_{x^2-y^2}$ type symmetry orbitals of the individual octahedra in the $a\text{-}b$ basal plane are orthogonal to each other. Jahn–Teller-active ions cause cooperative antiferrodistortive arrangements of the neighboring orthogonal octahedra, which produces ferromagnetic interactions. In fact, the system shows characteristics of a 2D Heisenberg ferromagnet.⁵⁰ The 2D copper halide perovskites presented herein are ideal model systems for the study of Jahn–Teller activity in Heisenberg systems, which may enable deeper understanding to the structure-magnetic relationships.⁵²

MChD is a magneto-optical effect in which the absorption coefficient of a chiral compound for an unpolarized light beam differs depending on whether an externally applied magnetic field is parallel or antiparallel to the propagation direction of the light beam.⁵³ MChD is described as a manifestation of magneto-chiral anisotropy, which can be formalized by expanding the frequency dependence (ω) of the absorption coefficient (ϵ) with magnetic field H and the light propagation vector κ (eq 2).

$$(\omega, \kappa, B) = \epsilon_0(\omega) \pm \alpha^{d/l}(\omega)\kappa \pm \beta(\omega)B \pm \gamma^{d/l}(\omega)\kappa \times B \quad (2)$$

Here, ϵ_0 is associated with the normal absorption of light at zero field, $\alpha^{d/l}$ to the natural circular dichroism, β to the magnetic circular dichroism, and $\gamma^{d/l}$ to the MChD, with d and l that refer to right- and left-handed medium, and \pm the right- and left-handed circularly polarized waves, respectively.⁵⁴ MChD signal is associated with spin excitations and can be used to probe molecular magnetism systems for store and read the information.^{55,56} Investigation on the microscopic origins of MChD from organic/inorganic hybrid materials is so far scarce and limited to only a few examples.^{53,54,57–59}

Owing to the coexistence of chirality and ferromagnetism, the two enantiomers of $(R\text{-MPEA})_2\text{CuCl}_4$ and $(S\text{-MPEA})_2\text{CuCl}_4$ are suitable for MChD study. The wavelength dependence of the optical transmission in the region of 200–900 nm with an applied magnetic field ($B = 1$ T) at 2 K was tested (Figure 4). Measurements performed in the same conditions for $(R\text{-MPEA})_2\text{CuCl}_4$ and $(S\text{-MPEA})_2\text{CuCl}_4$ provide several strong MChD signals with opposite signs in their optical response, resulting in perfect mirror images. The maximum absolute ΔA value of these perovskite chiral ferromagnets is around $1.9 \times 10^{-3} \text{ cm}^{-1}$, which is similar to that observed on Prussian blue analogue.⁵

Sharp MChD peaks are discernible at $\lambda = 262$ and 490 nm, as well as $\lambda = 545$ and 764 nm, corresponding to intra-atomic $d-d$ transitions in the Cu^{2+} ions.^{60,61} The inset shows the energy level diagram of d -orbitals for Cu^{2+} . According to ligand field theory, the ground state electronic distribution of Cu^{2+} is $t_{2g}^6 e_g^3$ which yields 2E_g term, where the excited electronic state is $t_{2g}^6 e_g^4$ which corresponds to $^2T_{2g}$ term.⁶² Due to Jahn–Teller effect, 2E_g ground state is split into $^2A_{1g}$ ($d_{x^2-y^2}$) and $^2A_{2g}$ (d_z^2), whereas $^2T_{2g}$ splits into $^2B_{1g}$ (d_{xy}), $^2B_{2g}$ (d_{xz}), and $^2B_{3g}$ (d_{yz}) states. In our case, the observed electronic transitions at 262, 490, and 764 nm for the two enantiomers can be assigned to the $^2A_{1g}$ ($d_{x^2-y^2}$) \rightarrow $^2B_{3g}$ (d_{yz}), $^2A_{1g}$ ($d_{x^2-y^2}$) \rightarrow $^2B_{2g}$ (d_{xz}), $^2A_{1g}$ ($d_{x^2-y^2}$) \rightarrow $^2A_{2g}$ (d_z^2), respectively. Figure 4 shows that the different transitions produce MChD signal is different in strength and line shape. The MChD signal around 545 nm

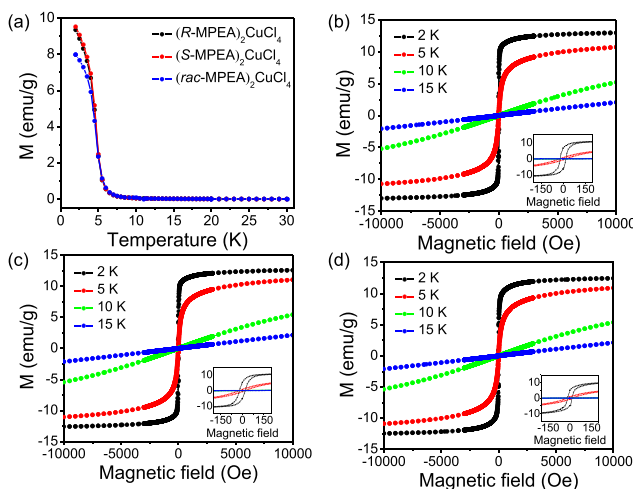


Figure 3. Magnetic properties of the $(R\text{-}, S\text{-}, rac\text{-MPEA})_2\text{CuCl}_4$. (a) Temperature dependence of the magnetizations of $(R\text{-MPEA})_2\text{CuCl}_4$, $(S\text{-MPEA})_2\text{CuCl}_4$, and $(rac\text{-MPEA})_2\text{CuCl}_4$ in applied fields of 100 Oe. (b–d) The hysteresis loops of $(R\text{-MPEA})_2\text{CuCl}_4$, $(S\text{-MPEA})_2\text{CuCl}_4$, and $(rac\text{-MPEA})_2\text{CuCl}_4$ at 2, 5, 10, and 15 K.

ferromagnetic ordering below 6 K was observed for $(R\text{-MPEA})_2\text{CuCl}_4$, $(S\text{-MPEA})_2\text{CuCl}_4$, and $(rac\text{-MPEA})_2\text{CuCl}_4$. The Curie temperatures of these 2D perovskites are similar to those observed on $(BED)_2\text{CuCl}_6$ ²³ and $\text{CuCl}_4(\text{C}_6\text{H}_5\text{CH}_2\text{CH}_2\text{NH}_3)_2$.⁴⁹ The hysteresis loops confirm the presence of spontaneous magnetization (Figure 3b–d). The magnetization nearly saturates at a value of 12.5 emu g^{-1} in a field of 2500 Oe at 2 K in all compounds. Furthermore, the ferromagnetic hysteresis loops show a quick saturation, therefore supporting the presence of significant interactions below the magnetic ordering transition.⁵⁰ When the temperature is higher than the Curie temperature, the hysteresis loops gradually disappear. It is noted that the saturated magnetization is the highest value in the ever reported in perovskite materials.

To date, only a few perovskite compounds have been reported to possess a ferromagnetic coupling. It is interesting to study the Jahn–Teller activity of Cu-based complexes in the

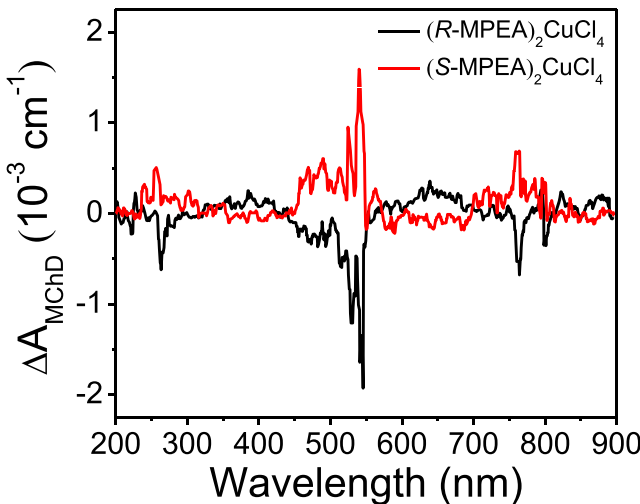


Figure 4. MChD investigation and the energy level diagram of *d*-orbitals for Cu^{2+} . MChD recorded on $(\text{R-MPEA})_2\text{CuCl}_4$ and $(\text{S-MPEA})_2\text{CuCl}_4$ at 2 K.

gives the strongest intensity, which is corresponding to the ${}^2\text{A}_{1g}$ ($d_{x^2-y^2}$) $\rightarrow {}^2\text{B}_{1g}$ (d_{xy}) transition,^{63,64} while the signals associated with the other transitions are less intense.

As discussed above, the orbitals on neighboring Cu^{2+} ions are orthogonal to each other, and the spins experience ferromagnetic superexchange interaction between Cu^{2+} ($S = 1/2$)⁶⁵ (Figure S4). In the UV-vis region, the MChD is generally understood as an interference effect between electric dipole (E_1) and magnetic dipole transitions (M_1) resulting from the SOC.^{66,67} On the basis of these mechanisms, the MChD signal of the *d*-*d* transition for Cu^{2+} is expressed by the summation of the $E_1 - M_1$ interference term of optical transition from the Cu^{2+} ions.⁶¹ Additionally, the dissymmetry factor for MChD can be defined as follows:

$$g_{\text{MChD}} = \frac{A(\mathbf{B} \uparrow \uparrow \boldsymbol{\kappa}) - A(\mathbf{B} \downarrow \uparrow \boldsymbol{\kappa})}{\frac{1}{2}(A(\mathbf{B} \uparrow \uparrow \boldsymbol{\kappa}) + A(\mathbf{B} \downarrow \uparrow \boldsymbol{\kappa}))} = 2 \frac{\Delta A_{\text{MChD}}}{A} \quad (3)$$

where $A = (A_- + A_+)/2$, A_- and A_+ are the absorbances for LCP and RCP in the absence of a magnetic field, respectively.⁵⁹ An essential characteristic of MChD is that g_{MChD} should be of opposite sign for two enantiomers.⁵⁹ We have calculated g_{MChD} between 250 and 500 nm according to eq 3. Figure S5 plots the experimental results for g_{MChD} against the wavelength for the two enantiomers, and the absolute values of the g_{MChD} are summarized in Table S5. We observed absolute values of $g_{\text{MChD}} = 0.51 \text{ T}^{-1}$ for the $(\text{R-MPEA})_2\text{CuCl}_4$ and $g_{\text{MChD}} = 0.59 \text{ T}^{-1}$ for $(\text{S-MPEA})_2\text{CuCl}_4$ at 405 nm, confirming significant magneto-chiral anisotropy.⁶⁸ It is noted that these g_{MChD} coefficients are much higher than that reported for $\text{Eu}((\pm)\text{tfc})_3$ complex ($5 \times 10^{-3} \text{ T}^{-1}$)⁵⁹ and chiral Ni nanomagnets⁶⁸ ($7.3 \times 10^{-4} \text{ T}^{-1}$). This intense absolute configuration-dependent signal is direct experimental proof of the existence of the MChD effect in these two perovskite materials.^{5,54}

In summary, we report the first pair of 2D hybrid perovskites that exhibit strong chirality and ferromagnetism simultaneously. Magnetic measurements reveal that these enantiomers have a saturation magnetization value up to 12.5 emu g^{-1} , which is the highest in the ever reported perovskite materials.

Moreover, this work presents the first successful MChD measurement in perovskite materials, which indicates that large values of magneto-chiral anisotropy can be obtained in perovskite chiral ferromagnets. Our results about MChD-featured chiral ferromagnets suggest that these materials hold potential for the development of magneto-optical devices, magneto-resistive sensors, and spintronic devices. This work provides a new strategy for creating novel chiral ferromagnets by exploiting the perovskite structure, which may lay a foundation for the further development of magnetic materials for spintronic applications.

EXPERIMENTAL SECTION

Materials. *R*-MPEA = *R*- β -methylphenethylamine (97%, ee 98%), *S*-MPEA = *S*- β -methylphenethylamine (97%, ee 98%) was purchased from Alfa Aesar. *rac*-MPEA = *rac*- β -methylphenethylamine (98%) was purchased from J&K Scientific Co., Ltd. $\text{CuCl}_2 \cdot 2\text{H}_2\text{O}$ (99.99%) was purchased from ALADDIN. Hydrochloric acid (36%–38%) was purchased from Xilong Chemical Reagent Co., Ltd. All reagents and solvents were used without further purification.

Synthesis of *R*-MPEA-HCl and *S*-MPEA-HCl Single Crystals.

R-MPEA-HCl was synthesized by reacting *R*-MPEA and hydrochloric acid with the molar ratio of 1:1. The hydrochloric acid was added dropwise into the *R*-MPEA in a single-mouth flask with a round-bottom in an ice bath. It takes an hour to complete. Then, the resulting solution was evaporated at 80°C in a rotary evaporator to remove the solvent. As the solvent is removed, a large number of solids appeared. The crystal was recrystallized in anhydrous ethanol two times, then dried in a vacuum oven at 60°C for 12 h. For the synthesis of *S*-MPEA-HCl, the steps were conducted using the same procedure as described above.

Synthesis of $(\text{R-MPEA})_2\text{CuCl}_4$ and $(\text{S-MPEA})_2\text{CuCl}_4$ Single Crystals. The synthesis of these enantiomeric crystals through self-assembly crystallization from an aqueous solution of chiral ammonium salt (*R*-MPEA-HCl and *S*-MPEA-HCl) and $\text{CuCl}_2 \cdot 2\text{H}_2\text{O}$ salts, by slowly cooling crystallization. Take $(\text{R-MPEA})_2\text{CuCl}_4$ as an example, *R*-MPEA-HCl and $\text{CuCl}_2 \cdot 2\text{H}_2\text{O}$ with the molar ratio of 2:1 were dissolved in an aqueous solution (2 mmol/mL) and stirred at 80°C for 20 min. Then, the clear solution was kept in a quiet environment without destabilization for slowly cooling from high temperature to low temperature. After about 2 h, many yellow plate-like crystals as large as several millimeters were obtained.

Synthesis of *rac*-MPEA-HCl and $(\text{rac-MPEA})_2\text{CuCl}_4$ Compounds. For the synthesis of *rac*-MPEA-HCl, the steps were conducted using the same procedure as that for the synthesis of *R*-MPEA-HCl and *S*-MPEA-HCl. By applying the racemic *rac*-MPEA-HCl in the synthesis, we also obtained a racemic compound $(\text{rac-MPEA})_2\text{CuCl}_4$. Although the crystal quality was not good enough for single-crystal structural analysis, we confirmed that $(\text{rac-MPEA})_2\text{CuCl}_4$ crystallizes in a different structure from those of $(\text{R-MPEA})_2\text{CuCl}_4$ and $(\text{S-MPEA})_2\text{CuCl}_4$ by comparing PXRD patterns (Figure S6).

Thermogravimetric Analyses (TGA). TGA was carried out on a Linseis STA PT1600. A heating rate of $10^\circ\text{C min}^{-1}$ under flowing N_2 was used from room temperature to high temperature to investigate the thermal stabilities.

Powder X-ray Diffraction (PXRD). The X-ray diffraction data were obtained at X'Pert PRO made by the Panalytical Company with a wavelength of 1.5406 \AA .

Single Crystal X-ray Diffraction (SCXRD). Single crystals of $(\text{R-MPEA})_2\text{CuCl}_4$ and $(\text{S-MPEA})_2\text{CuCl}_4$ with good quality were carried out on a Bruker D8 VENTURE Kappa Duo PHOTON II CPAD diffractometer with graphite-monochromatized $\text{Cu K}\alpha$ radiation ($\lambda = 1.54184 \text{ \AA}$), operating at 50 kV and 40 mA under N_2 flow. Crystal data were integrated and corrected for absorption (numerical) using the STOE X-AREA programs. Crystal structures were solved by direct methods and refined by full-matrix least-squares on F^2 using the OLEX2 program package.

Circular Dichroism Spectra. The CD spectra were collected using a CD spectrometer (J-1500, JASCO) at room temperature. KBr pellets were employed as the matrix for performing solid-state CD measurements.

Magnetic Measurement. The magnetic properties of the powdered samples were measured using a superconducting quantum interference device magnetometer with a sensitivity better than 10^{-8} emu (Quantum Design MPMS-XL, U.S.A.).

Magneto-Chiral Dichroism. Manual grinding powder form (*R*-MPEA)₂CuCl₄ and (*S*-MPEA)₂CuCl₄ mm-sized crystals were used for magneto-chiral dichroism investigation. Magneto-chiral dichroism spectra measurements were made on Applied Photophysics Chirascan Magnetic circular dichroism spectrometer in the presence of a magnetic field with both parallel and antiparallel fields. Unpolarized light was directed onto the samples using optical fibers. The two beams of circularly polarized light with left and right rotation are monochromated and focused. After that, the sample has the same energy, the same light intensity, the same circular degree of polarization, the same spot size, and the same position. The wavelength dependence of the optical transmission in the region of 200–900 nm with an applied magnetic field ($B = 1$ T) at 2 K was measured. The sample is placed in a cryostat, and the cooling rate is 5 °C/min. The averaged magneto-chiral dichroism spectra were obtained from the difference between the parallel and antiparallel transmission spectra.

■ ASSOCIATED CONTENT

SI Supporting Information

The Supporting Information is available free of charge at <https://pubs.acs.org/doi/10.1021/acs.chemmater.0c02729>.

TGA; Photoluminescence spectra; CD spectra; configuration of Cu $d_{x^2-y^2}$ orbital; crystal data and structure refinement of (*R*-MPEA)₂CuCl₄ and (*S*-MPEA)₂CuCl₄; distortions of CuCl₆ octahedral; and summary of the $l_{g_{\text{MChD}}}$ (PDF)

X-ray crystallographic file for (*R*-MPEA)₂CuCl₄ (CIF)

X-ray crystallographic file for (*S*-MPEA)₂CuCl₄ (CIF)

■ AUTHOR INFORMATION

Corresponding Authors

Xiangfeng Shao — State Key Laboratory of Applied Organic Chemistry (SKLAOC), Key Laboratory of Special Function Materials and Structure Design (MOE), College of Chemistry and Chemical Engineering, Lanzhou University, Lanzhou 730000, P. R. China; orcid.org/0000-0002-8710-4122; Email: shaoxf@lzu.edu.cn

Dezheng Yang — Key Laboratory for Magnetism and Magnetic Materials of Ministry of Education, School of Physical Science and Technology, Lanzhou University, Lanzhou 730000, P. R. China; Email: yangdzh@lzu.edu.cn

Hao-Li Zhang — State Key Laboratory of Applied Organic Chemistry (SKLAOC), Key Laboratory of Special Function Materials and Structure Design (MOE), College of Chemistry and Chemical Engineering, Lanzhou University, Lanzhou 730000, P. R. China; Tianjin Key Laboratory of Molecular Optoelectronic Sciences, Collaborative Innovation Center of Chemical Science and Engineering, Tianjin University, Tianjin 300072, P. R. China; orcid.org/0000-0002-6322-5202; Email: haoli.zhang@lzu.edu.cn

Authors

Bing Sun — State Key Laboratory of Applied Organic Chemistry (SKLAOC), Key Laboratory of Special Function Materials and Structure Design (MOE), College of Chemistry and Chemical

Engineering, Lanzhou University, Lanzhou 730000, P. R. China

Xiao-Fei Liu — State Key Laboratory of Applied Organic Chemistry (SKLAOC), Key Laboratory of Special Function Materials and Structure Design (MOE), College of Chemistry and Chemical Engineering, Lanzhou University, Lanzhou 730000, P. R. China

Xiang-Yang Li — State Key Laboratory of Applied Organic Chemistry (SKLAOC), Key Laboratory of Special Function Materials and Structure Design (MOE), College of Chemistry and Chemical Engineering, Lanzhou University, Lanzhou 730000, P. R. China

Yamin Zhang — State Key Laboratory of Applied Organic Chemistry (SKLAOC), Key Laboratory of Special Function Materials and Structure Design (MOE), College of Chemistry and Chemical Engineering, Lanzhou University, Lanzhou 730000, P. R. China

Complete contact information is available at:
<https://pubs.acs.org/10.1021/acs.chemmater.0c02729>

Notes

The authors declare no competing financial interest.

■ ACKNOWLEDGMENTS

This work was supported by the National Key R&D Program of China (2017YFA0204903), National Natural Science Foundation of China (NSFC. S1733004, S1525303, 1522203), 111 Project, and the Fundamental Research Funds for the Central Universities. The authors thank beamline BL14B1 (Shanghai Synchrotron Radiation Facility) for providing the beam time.

■ REFERENCES

- (1) Naaman, R.; Paltiel, Y.; Waldeck, D. H. Chiral molecules and the electron spin. *Nat. Rev. Chem.* **2019**, *3*, 250–260.
- (2) Ohkoshi, S.-I.; Takano, S.; Imoto, K.; Yoshikiyo, M.; Namai, A.; Tokoro, H. 90-degree optical switching of output second-harmonic light in chiral photomagnet. *Nat. Photonics* **2014**, *8*, 65–71.
- (3) Li, Q.; Kharzeev, D. E.; Zhang, C.; Huang, Y.; Pletikosić, I.; Fedorov, A. V.; Zhong, R. D.; Schneeloch, J. A.; Gu, G. D.; Valla, T. Chiral magnetic effect in ZrTe₅. *Nat. Phys.* **2016**, *12*, 550–554.
- (4) Lu, H.; Wang, J.; Xiao, C.; Pan, X.; Chen, X.; Brunecky, R.; Berry, J. J.; Zhu, K.; Beard, M. C.; Vardeny, Z. V. Spin-dependent charge transport through 2D chiral hybrid lead-iodide perovskites. *Sci. Adv.* **2019**, *5*, No. eaay0571.
- (5) Atzori, M.; Breslavetz, I.; Paillot, K.; Inoue, K.; Rikken, G.; Train, C. A Chiral Prussian Blue Analogue Pushes Magneto-Chiral Dichroism Limits. *J. Am. Chem. Soc.* **2019**, *141*, 20022–20025.
- (6) Jué, E.; Safeer, C. K.; Drouard, M.; Lopez, A.; Balint, P.; Budapestebau, L.; Boulle, O.; Auffret, S.; Schuh, A.; Manchon, A.; Miron, I. M.; Gaudin, G. Chiral damping of magnetic domain walls. *Nat. Mater.* **2016**, *15*, 272–277.
- (7) Bode, M.; Heide, M.; von Bergmann, K.; Ferriani, P.; Heinze, S.; Bihlmayer, G.; Kubetzka, A.; Pietzsch, O.; Blugel, S.; Wiesendanger, R. Chiral magnetic order at surfaces driven by inversion asymmetry. *Nature* **2007**, *447*, 190–193.
- (8) Onoda, S.; Nagaosa, N. Spin chirality fluctuations and anomalous Hall effect in itinerant ferromagnets. *Phys. Rev. Lett.* **2003**, *90*, 196602.
- (9) Champel, T.; Lofwander, T.; Eschrig, M. O- π Transitions in a superconductor/chiral ferromagnet/superconductor junction induced by a homogeneous cycloidal spiral. *Phys. Rev. Lett.* **2008**, *100*, 077003.
- (10) Chauleau, J. Y.; Chirac, T.; Fusil, S.; Garcia, V.; Akhtar, W.; Tranchida, J.; Thibaudeau, P.; Gross, I.; Blouzon, C.; Finco, A.; Bibes, M.; Dkhil, B.; Khalyavin, D. D.; Manuel, P.; Jacques, V.; Jaouen, N.;

- Viret, M. Electric and antiferromagnetic chiral textures at multiferroic domain walls. *Nat. Mater.* **2020**, *19*, 386–390.
- (11) Wang, Z.; Gao, M.; Wei, M.; Ren, S.; Hao, X. T.; Qin, W. Organic Chiral Charge Transfer Magnets. *ACS Nano* **2019**, *13*, 4705–4711.
- (12) Beghidja, A.; Rogez, G.; Rabu, P.; Welter, R.; Drillon, M. An approach to chiral magnets using α -hydroxycarboxylates. *J. Mater. Chem.* **2006**, *16*, 2715–2728.
- (13) Coronado, E.; Gómez-García, C. J.; Nuez, A.; Romero, F. M.; Waerenborgh, J. C. Synthesis, Chirality, and Magnetic Properties of Bimetallic Cyanide-Bridged Two-Dimensional Ferromagnets. *Chem. Mater.* **2006**, *18*, 2670–2681.
- (14) Hou, S. Z.; Cao, D. K.; Li, Y. Z.; Zheng, L. M. Chiral-layered metal phosphonate formed via spontaneous resolution showing dehydration-induced antiferromagnetic to ferromagnetic transformation. *Inorg. Chem.* **2008**, *47*, 10211–10213.
- (15) Train, C.; Gheorghe, R.; Krstic, V.; Chamoreau, L. M.; Ovanesyan, N. S.; Rikken, G. L.; Gruselle, M.; Verdaguier, M. Strong magneto-chiral dichroism in enantiopure chiral ferromagnets. *Nat. Mater.* **2008**, *7*, 729–734.
- (16) Zhang, Y.; Liu, Y.; Xu, Z.; Ye, H.; Yang, Z.; You, J.; Liu, M.; He, Y.; Kanatzidis, M. G.; Liu, S. F. Nucleation-controlled growth of superior lead-free perovskite $\text{Cs}_3\text{Bi}_2\text{I}_9$ single-crystals for high-performance X-ray detection. *Nat. Commun.* **2020**, *11*, 2304.
- (17) Rabu, P.; Drillon, M. Layered Organic-Inorganic Materials: A Way towards Controllable Magnetism. *Adv. Eng. Mater.* **2003**, *5*, 189–210.
- (18) Huang, B.; Wang, B. Y.; Du, Z. Y.; Xue, W.; Xu, W. J.; Su, Y. J.; Zhang, W. X.; Zeng, M. H.; Chen, X. M. Importing spontaneous polarization into a Heisenberg ferromagnet for a potential single-phase multiferroic. *J. Mater. Chem. C* **2016**, *4*, 8704–8710.
- (19) Xiong, R. G.; Lu, S. Q.; Zhang, Z. X.; Cheng, H.; Li, P. F.; Liao, W. Q. A Chiral Thermochromic Ferroelastic with Seven Physical Channel Switches. *Angew. Chem., Int. Ed.* **2020**, *59*, 9574–9578.
- (20) Yuan, Y.; Liu, X. F.; Ma, X.; Wang, X.; Li, X.; Xiao, J.; Li, X.; Zhang, H. L.; Wang, L. Large Band Gap Narrowing and Prolonged Carrier Lifetime of $(\text{C}_4\text{H}_9\text{NH}_3)_2\text{PbI}_4$ under High Pressure. *Adv. Sci. Sci.* **2019**, *6*, 1900240.
- (21) Schmitt, T.; Bourelle, S.; Tye, N.; Soavi, G.; Bond, A. D.; Feldmann, S.; Traore, B.; Katan, C.; Even, J.; Dutton, S. E.; Deschler, F. Control of Crystal Symmetry Breaking with Halogen-Substituted Benzylammonium in Layered Hybrid Metal-Halide Perovskites. *J. Am. Chem. Soc.* **2020**, *142*, 5060–5067.
- (22) Huang, B.; Zhang, J. Y.; Huang, R. K.; Chen, M. K.; Xue, W.; Zhang, W. X.; Zeng, M. Y.; Chen, X. M. Spin-reorientation-induced magnetodielectric coupling effects in two layered perovskite mag-nets. *Chem. Sci.* **2018**, *9*, 7413–7418.
- (23) Sun, B.; Liu, X. F.; Li, X. Y.; Cao, Y.; Yan, Z.; Fu, L.; Tang, N.; Wang, Q.; Shao, X.; Yang, D.; Zhang, H. L. Reversible Thermochromism and Strong Ferromagnetism in Two-Dimensional Hybrid Perovskites. *Angew. Chem., Int. Ed.* **2020**, *59*, 203–208.
- (24) Long, G. K.; Sabatini, R.; Saidaminov, M. I.; Lakhwani, G.; Rasmita, A.; Liu, X. G.; Sargent, E. H.; Gao, W. B. Chiral-perovskite optoelectronics. *Nat. Rev. Mater.* **2020**, *5*, 423–439.
- (25) Ahn, J.; Ma, S.; Kim, J. Y.; Kyhm, J.; Yang, W.; Lim, J. A.; Kotov, N. A.; Moon, J. Chiral 2D Organic Inorganic Hybrid Perovskite with Circular Dichroism Tunable Over Wide Wavelength Range. *J. Am. Chem. Soc.* **2020**, *142*, 4206–4212.
- (26) Yang, C. K.; Chen, W. N.; Ding, Y. T.; Wang, J.; Rao, Y.; Liao, W. Q.; Tang, Y. Y.; Li, P. F.; Wang, Z. X.; Xiong, R. G. The First 2D Homochiral Lead Iodide Perovskite Ferroelectrics: [R- and S-1-(4-Chlorophenyl)ethylammonium]₂PbI₄. *Adv. Mater.* **2019**, *31*, 1808088.
- (27) Tang, Y. Y.; Ai, Y.; Liao, W. Q.; Li, P. F.; Wang, Z. X.; Xiong, R. G. H/F-Substitution-Induced Homochirality for Designing High-T_c Molecular Perovskite Ferroelectrics. *Adv. Mater.* **2019**, *31*, 1902163.
- (28) Ai, Y.; Chen, X. G.; Shi, P. P.; Tang, Y. Y.; Li, P. F.; Liao, W. Q.; Xiong, R. G. Fluorine Substitution Induced High T_c of Enantiomeric Perovskite Ferroelectrics: (R)- and (S)-3-(Fluoropyrrolidinium)MnCl₃. *J. Am. Chem. Soc.* **2019**, *141*, 4474–4479.
- (29) Long, G.; Jiang, C.; Sabatini, R.; Yang, Z.; Wei, M.; Quan, L. N.; Liang, Q.; Rasmita, A.; Askerka, M.; Walters, G.; Gong, X.; Xing, J.; Wen, X.; Quintero-Bermudez, R.; Yuan, H.; Xing, G.; Wang, X. R.; Song, D.; Voznyy, O.; Zhang, M.; Hoogland, S.; Gao, W.; Xiong, Q.; Sargent, E. H. Spin control in reduced-dimensional chiral perovskites. *Nat. Photonics* **2018**, *12*, 528–533.
- (30) Zhang, C.; Sun, D.; Vardeny, Z. V. Multifunctional Optoelectronic-Spintronic Device Based on Hybrid Organometal Trihalide Perovskites. *Adv. Electron. Mater.* **2017**, *3*, 1600426.
- (31) Zhai, Y.; Baniya, S.; Zhang, C.; Li, J.; Haney, P.; Sheng, C. X.; Ehrenfreund, E.; Vardeny, Z. V. Giant Rashba splitting in 2D organic-inorganic halide perovskites measured by transient spectroscopies. *Sci. Adv.* **2017**, *3*, e1700704.
- (32) Niesner, D.; Wilhelm, M.; Levchuk, I.; Osvet, A.; Shrestha, S.; Batentschuk, M.; Brabec, C.; Fauster, T. Giant Rashba Splitting in $\text{CH}_3\text{NH}_3\text{PbBr}_3$ Organic-Inorganic Perovskite. *Phys. Rev. Lett.* **2016**, *117*, 126401.
- (33) Yang, Y.; Yang, M.; Zhu, K.; Johnson, J. C.; Berry, J. J.; van de Lagemaat, J.; Beard, M. C. Large polarization-dependent exciton optical Stark effect in lead iodide perovskites. *Nat. Commun.* **2016**, *7*, 12613.
- (34) Giovanni, D.; Chong, W. K.; Dewi, H. A.; Thirumal, K.; Ne-Ogi, I.; Ramesh, R.; Mhaisalkar, S.; Mathews, N.; Sum, T. C. Tunable room-temperature spin-selective optical Stark effect in solution-processed layered halide perovskites. *Sci. Adv.* **2016**, *2*, No. e1600477.
- (35) Giovanni, D.; Ma, H.; Chua, J.; Gratzel, M.; Ramesh, R.; Mhaisalkar, S.; Mathews, N.; Sum, T. C. Highly spin-polarized carrier dynamics and ultralarge photoinduced magnetization in $\text{CH}_3\text{NH}_3\text{PbI}_3$ perovskite thin films. *Nano Lett.* **2015**, *15*, 1553–1558.
- (36) Long, G.; Zhou, Y.; Zhang, M.; Sabatini, R.; Rasmita, A.; Huang, L.; Lakhwani, G.; Gao, W. Theoretical Prediction of Chiral 3D Hybrid Organic-Inorganic Perovskites. *Adv. Mater.* **2019**, *31*, 1807628.
- (37) Gunasekera, J.; Dahal, A.; Chen, Y.; Rodriguez-Rivera, J. A.; Harriger, L. W.; Thomas, S.; Heitmann, T. W.; Dugaev, V.; Ernst, A.; Singh, D. K. Quantum Magnetic Properties in Perovskite with Anderson Localized Artificial Spin-1/2. *Adv. Sci.* **2018**, *5*, 1700978.
- (38) Liu, X.; Chanana, A.; Huynh, U.; Xue, F.; Haney, P.; Blair, S.; Jiang, X.; Vardeny, Z. V. Circular photogalvanic spectroscopy of Rashba splitting in 2D hybrid organic-inorganic perovskite multiple quantum wells. *Nat. Commun.* **2020**, *11*, 323.
- (39) Caretta, A.; Miranti, R.; Arkenbout, A. H.; Polyakov, A. O.; Meetsma, A.; Hidayat, R.; Tjia, M. O.; Palstra, T. T.; van Loosdrecht, P. H. Thermochromic effects in a Jahn-Teller active CuCl_6^{4-} layered hybrid system. *J. Phys.: Condens. Matter* **2013**, *25*, 505901.
- (40) Mao, L.; Guo, P.; Kepenekian, M.; Hadar, I.; Katan, C.; Even, J.; Schaller, R. D.; Stoumpos, C. C.; Kanatzidis, M. G. Structural Diversity in White-Light-Emitting Hybrid Lead Bromide Perovskites. *J. Am. Chem. Soc.* **2018**, *140*, 13078–13088.
- (41) Jaffe, A.; Lin, Y.; Mao, W. L.; Karunadasa, H. I. Pressure-Induced Conductivity and Yellow-to-Black Piezochromism in a Layered Cu-Cl Hybrid Perovskite. *J. Am. Chem. Soc.* **2015**, *137*, 1673–1678.
- (42) Mao, L.; Wu, Y.; Stoumpos, C. C.; Traore, B.; Katan, C.; Even, J.; Wasielewski, M. R.; Kanatzidis, M. G. Tunable White-Light Emission in Single-Cation-Templated Three-Layered 2D Perovskites $(\text{CH}_3\text{CH}_2\text{NH}_3)_4\text{Pb}_3\text{Br}_{10-x}\text{Cl}_x$. *J. Am. Chem. Soc.* **2017**, *139*, 11956–11963.
- (43) Spanopoulos, I.; Hadar, I.; Ke, W.; Tu, Q.; Chen, M.; Tsai, H.; He, Y.; Shekhawat, G.; Dravid, V. P.; Wasielewski, M. R.; Mohite, A. D.; Stoumpos, C. C.; Kanatzidis, M. G. Uniaxial Expansion of the 2D Ruddlesden-Popper Perovskite Family for Improved Environmental Stability. *J. Am. Chem. Soc.* **2019**, *141*, 5518–5534.
- (44) Bailey, N. A.; Fenton, D. E.; Moody, R.; de Barbarin, C. O. R.; Sciambarella, I. N.; Latour, J. M.; Limosin, D.; McKee, V. Complexes of ligands providing endogenous bridges. Part 4. Copper(II) complexes of macrocyclic Schiff bases derived from 2,6-diacylpyr-

- idine and 1, n-diamino-n'-hydroxyalkanes ($n, n' = 3, 2; 4, 2;$ and $5, 3$): synthesis, properties, and structures. *J. Chem. Soc., Dalton Trans.* **1987**, *11*, 2519–2529.
- (45) Zhu, X.; Xu, H.; Liu, Y.; Zhang, J.; Wang, M.; Ivanov, I. N.; Ovchinnikova, O. S.; Hu, B. Two-Photon Up-Conversion Photoluminescence Realized through Spatially Extended Gap States in Quasi-2D Perovskite Films. *Adv. Mater.* **2019**, *31*, 1901240.
- (46) Jaffe, A.; Mack, S. A.; Lin, Y.; Mao, W. L.; Neaton, J. B.; Karunadasa, H. I. High Compression-Induced Conductivity in a Layered Cu-Br Perovskite. *Angew. Chem., Int. Ed.* **2020**, *59*, 4017–4022.
- (47) Desjardins, S. R.; Penfield, K. W.; Cohen, S. L.; Musselman, R. L.; Solomon, E. I. Detailed Absorption, Reflectance, and UV Photoelectron Spectroscopic and Theoretical Studies of the Charge-Transfer Transitions of CuCl_4^{2-} : Correlation of the Square-Planar and the Tetrahedral Limits. *J. Am. Chem. Soc.* **1983**, *105*, 4590–4603.
- (48) Wang, L.; Xue, Y.; Cui, M.; Huang, Y.; Xu, H.; Qin, C.; Yang, J.; Dai, H.; Yuan, M. A Chiral Reduced-Dimension Perovskite for an Efficient Flexible Circularly Polarized Light Photodetector. *Angew. Chem., Int. Ed.* **2020**, *59*, 6442–6450.
- (49) Polyakov, A. O.; Arkenbout, A. H.; Baas, J.; Blake, G. R.; Meetsma, A.; Caretta, A.; van Loosdrecht, P. H. M.; Palstra, T. T. M. Coexisting Ferromagnetic and Ferroelectric Order in a CuCl_4 -based Organic-Inorganic Hybrid. *Chem. Mater.* **2012**, *24*, 133–139.
- (50) Kundys, B.; Lappas, A.; Viret, M.; Kapustianyk, V.; Rudyk, V.; Semak, S.; Simon, C.; Bakaimi, I. Multiferroicity and hydrogen-bond ordering in $(\text{C}_2\text{H}_5\text{NH}_3)_2\text{CuCl}_4$ featuring dominant ferromagnetic interactions. *Phys. Rev. B: Condens. Matter Mater. Phys.* **2010**, *81*, 224434.
- (51) Aqeel, A.; Akhtar, N.; Polyakov, A. O.; Rudolf, P.; Palstra, T. T. M. Magnetic functionality of thin film perovskite hybrids. *APL Mater.* **2018**, *6*, 114206.
- (52) Park, S. H.; Oh, I. H.; Park, S.; Park, Y.; Kim, J. H.; Huh, Y. D. Canted antiferromagnetism and spin reorientation transition in layered inorganic-organic perovskite $(\text{C}_6\text{H}_5\text{CH}_2\text{CH}_2\text{NH}_3)_2\text{MnCl}_4$. *Dalton Trans.* **2012**, *41*, 1237–1242.
- (53) Sessoli, R.; Boulon, M. E.; Caneschi, A.; Mannini, M.; Poggini, L.; Wilhelm, F.; Rogalev, A. Strong magneto-chiral dichroism in a paramagnetic molecular helix observed by hard X-ray. *Nat. Phys.* **2015**, *11*, 69–74.
- (54) Atzori, M.; Rikken, G.; Train, C. Magneto-Chiral Dichroism: A Playground for Molecular Chemists. *Chem.—Eur. J.* **2020**, *26*, 9784.
- (55) Bordács, S.; Kézsmárki, I.; Szaller, D.; Demkó, L.; Kida, N.; Murakawa, H.; Onose, Y.; Shimano, R.; Rööm, T.; Nagel, U.; Mi-Yahara, S.; Furukawa, N.; Tokura, Y. Chirality of matter shows up via spin excitations. *Nat. Phys.* **2012**, *8*, 734–738.
- (56) Train, C.; Gruselle, M.; Verdaguera, M. The fruitful introduction of chirality and control of absolute configurations in molecular magnets. *Chem. Soc. Rev.* **2011**, *40*, 3297–3312.
- (57) Ceolin, M.; Goberna-Ferron, S.; Galan-Mascaro, J. R. Strong hard X-ray magnetochiral dichroism in paramagnetic enantiopure molecules. *Adv. Mater.* **2012**, *24*, 3120–3123.
- (58) Kitagawa, Y.; Segawa, H.; Ishii, K. Magneto-chiral dichroism of organic compounds. *Angew. Chem., Int. Ed.* **2011**, *50*, 9133–9136.
- (59) Rikken, G. L. J. A.; Raupach, E. Observation of magneto-chiral dichroism. *Nature* **1997**, *390*, 493–494.
- (60) Saito, M.; Ishikawa, K.; Taniguchi, K.; Arima, T. Magnetic control of crystal chirality and the existence of a large magneto-optical dichroism effect in CuB_2O_4 . *Phys. Rev. Lett.* **2008**, *101*, 117402.
- (61) Taniguchi, K.; Kishiu, S.; Kimura, S.; Miyasaka, H. Local-Site Dependency of Magneto-Chiral Dichroism in Enantiopure One-Dimensional Copper(II)-Chromium(III) Coordination Polymers. *J. Phys. Soc. Jpn.* **2019**, *88*, 093708.
- (62) Reddy, S. L.; Endo, T.; Reddy, G. S. Electronic (Absorption) Spectra of 3d Transition Metal Complexes. In *Advanced Aspects of Spectroscopy*; M. A. Farrukh/IntechOpen, 2012; Chapter 1, pp 4–48.
- (63) Jianmin, L.; Yugeng, Z. The d-d Transition Spectra of Copper (II) Complexes in Different Coordination Environment. Study on $\text{Cu}(\text{TTA})_2$ and $\text{Cu}_2(\text{sacch})_4(\text{Im})_4$. *Cryst. Res. Technol.* **1991**, *26*, 331–337.
- (64) Savithri, K.; Kumar, B. C. V.; Vivek, H. K.; Revanasiddappa, H. D. Synthesis and Characterization of Cobalt(III) and Copper(II) Complexes of 2-((E)-(6-Fluorobenzo[d]thiazol-2-ylimino) methyl)-4-chlorophenol: DNA Binding and Nuclease Studies-SOD and Antimicrobial Activities. *Int. J. Spectrosc.* **2018**, *2018*, 1–15.
- (65) Khomskii, D. I.; Kugel, K. I. Orbital and magnetic structure of two-dimensional ferromagnets with Jahn-Teller ions. *Solid State Commun.* **1973**, *13*, 763–766.
- (66) Barron, L. D.; Vrbancich, J. Magneto-chiral birefringence and dichroism. *Mol. Phys.* **1984**, *51*, 715–730.
- (67) Taniguchi, K.; Nishio, M.; Kishiu, S.; Huang, P.-J.; Kimura, S.; Miyasaka, H. Strong magnetochiral dichroism for visible light emission in a rationally designed paramagnetic enantiopure molecule. *Phys. Rev. Mater.* **2019**, *3*, 045202.
- (68) Eslami, S.; Gibbs, J. G.; Reckkemmer, Y.; van Slageren, J.; Alarcón-Correia, M.; Lee, T.-C.; Mark, A. G.; Rikken, G. L. J. A.; Fischer, P. Chiral Nanomagnets. *ACS Photonics* **2014**, *1*, 1231–1236.